Interfacial Heat Transport via Evanescent Radiation by Hot Electrons

William D. Hutchins,[1,*] Saman Zare,[1,*] Mehran Habibzadeh,[2] Sheila Edalatpour,[2] and Patrick E. Hopkins[1,3,4,†]
[1]Department of Mechanical and Aerospace Engineering, University of Virginia, Charlottesville, Virginia 22904, USA
[2]Department of Mechanical Engineering, University of Maine, Orono, Maine 04469, USA
[3]Department of Materials Science and Engineering, University of Virginia, Charlottesville, Virginia 22904, USA
[4]Department of Physics, University of Virginia, Charlottesville, Virginia 22904, USA

(Received 4 November 2024; revised 29 January 2025; accepted 7 April 2025; published 8 May 2025)

We predict an additional thermal transport pathway across metal-nonmetal interfaces with large electron-phonon nonequilibrium via evanescent radiative heat transfer. In such systems, electron scattering processes vary drastically and can be leveraged to guide heat across interfaces via radiative heat transport without engaging the lattice directly. We employ the formalism of fluctuational electrodynamics to simulate the spectral radiative heat flux across the interface of a metal film and a nonmetal substrate. We find that the radiative conductance can exceed 300 MW m^{-2} K^{-1} at an electron temperature of 5000 K for an emitting tungsten film on a hexagonal boron nitride substrate, becoming comparable to its conductive counterpart. This allows for a more holistic approach to the heat flow across interfaces, accounting for electron-phonon nonequilibrium and ultrafast near-field phonon-polariton coupling.

DOI: 10.1103/PhysRevLett.134.186302

The thermal boundary conductance (TBC) between two solids relates the heat flux, q, to the temperature drop ΔT across the interface. Over the past few decades, theories that describe the interactions among electrons and phonons at interfaces have elucidated various fundamental carrier scattering and conversion processes that drive these interfacial thermal transport pathways [1–6].

One of the most fundamental and ubiquitous transfer mechanisms, thermal radiation, has been neglected in this interfacial heat transfer discussion and concomitant thermal boundary conductance theories. The relatively small fluxes inhibited by the blackbody limit seem negligible when compared to traditionally studied conductive pathways driven by electrons and phonons. In recent years, there has been a renewed interest in this field due to the verification of the prediction of super Planckian enhancement due to the contribution of evanescent modes [7–9]. This is of special importance in the "near-field" regime, when the separation distances are smaller than the thermal wavelength [10]. The contribution of evanescent radiative modes can be the dominant thermal transport mechanism within these distances [11]. With the ability of evanescent radiative heat transfer (RHT) to exceed the blackbody limit, many experiments have been performed for a range of different geometries, materials, and gaps ranging from micrometers down to nanometers [12,13]. Due to this new capability, there is growing interest in the effect that evanescent RHT can have on various thermal technologies such as thermophotovoltaics [14], heat-assisted magnetic recording devices [15,16], scanning thermal microscopy [17,18], and coherent thermal sources [19–21]. Hence, we must envelop our standard thermal theory of interfacial transport [1] to leverage evanescent RHT in the solid state.

The largest RHT enhancements in natural materials have been reported in polar dielectrics, such as SiC, SiO_2, and hBN, where phonon polariton dominate the evanescent modes [22,23] in the near field as predicted via Rytov's formalism of fluctuational electrodynamics [24,25]. This theory predicts thermal radiation mediated by all propagative, frustrated and surface modes at an arbitrary distance from an emitting body. The frustrated and surface modes are not allowed to propagate outside the emitting body (i.e., they are evanescent), as the parallel component of the wave vector (k_ρ) for these modes is greater than the free-space wave vector (k_0). However, when another medium is brought close to this body, the evanescent modes can be coupled to the receiving system, and the heat is transported radiatively. The interfaces adjacent to polar dielectric systems are also the source of major thermal boundary resistances due to the large phononic mismatches that occur at metal-dielectric interfaces in devices [6,26], thus heavily reducing the possible thermal management at these scales. To compound this, the electrons of metal interconnects are often an order of magnitude hotter than the phonon subsystem during operation [27]. Capitalizing on evanescent RHT, the thermal boundary conductance across metal-dielectric interfaces can be tuned by using the electron-phonon nonequilibrium.

In this Letter, we model the transduction of thermal radiation from a metallic emitter into an insulating

*These authors contributed equally to this work.
†Corresponding author: phopkins@virginia.edu

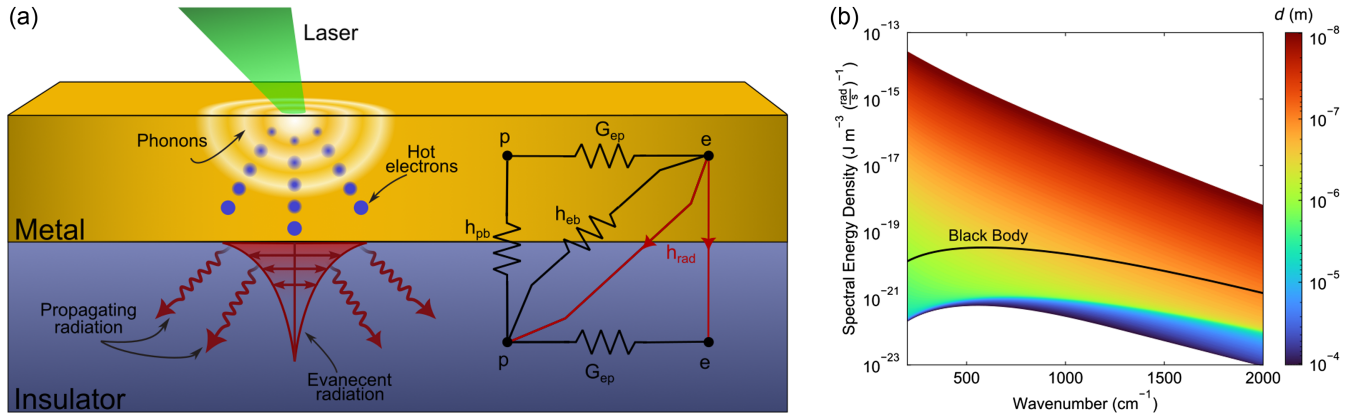

FIG. 1. (a) Diagram of interfacial transport phenomena. The schematic depicts energy transfer processes between electrons (e), phonons (p), and boundary (b) immediately after an ultrashort laser pulse is absorbed. The evanescent and propagating radiation due to ballistic hot electrons is absorbed into the substrate based on the dielectric properties beneath the interface. (b) The spectral energy density due to radiation of propagating and evanescent modes from a gold film at a distance d (shown in the color bar) away from the surface calculated using FED. The solid black line shows the far-field blackbody limit.

dielectric substrate, specifically under the case of strong electron-phonon nonequilibrium. By leveraging the formalism of fluctuational electrodynamics (FED) as well as the classic Drude-Sommerfeld theory of free electrons [28], we also examine the effect of electron temperature in the metallic thin film on interfacial radiative conductance, h_{rad}, in the presence of polaritonic and hyperbolic insulators. By doing so, we demonstrate that there can be more than twofold increases in overall thermal interfacial transport at high electron temperatures due to the contribution of evanescent radiative heat flux at metal-insulator interfaces.

The configuration studied here is schematically depicted in Fig. 1(a), where nonequilibrium is illustrated as the separation in thermal energy immediately after excitation from short pulsed laser absorption. Another example of this nonequilibrium occurs in the gate of high-frequency electronic devices [21,29,30]. These events can cause the electronic bath at temperatures of thousands of Kelvin while maintaining a cold lattice. This nonequilibrium manifests as the opening up of the Fermi surfaces, resulting in an increase in the population and the scattering rates of conducting electrons [3,31–33]. These increases open up possible radiative photonic states in both the propagating and evanescent regions of the photonic dispersion. The proposed mechanism of RHT across interfaces is fueled by the absorption in insulating dielectrics. These dielectric materials with high indices can shuttle the evanescent modes from the metal into high-wave-vector photonic states, enhancing thermal transport.

All the processes of the thermal transfer across the interface are depicted in Fig. 1(a), where "e" and "p" refer to the electronic and phononic subsystems, respectively. Each material has its electron-phonon coupling rate, G_{ep} [34], at which electronic energy is converted to phonon energy. The conductance across the interface includes the phonon contribution to the boundary resistance (h_{pb}) [1] and the contribution associated with electron collisions at the interface producing phonons in the insulator (h_{eb}) [35]. Finally, there exists a conductance associated with the mechanism proposed by this work, where the thermal radiation emitted by the electrons may be absorbed into the phonons or electrons in the substrate (h_{rad}). To represent the scale of available energy contained in thermally excited evanescent modes of a metallic emitter, we calculate the energy density at a distance d away from a gold layer with bulk properties [Fig. 1(b)] using FED [8,25,36]. As d decreases, the emitted flux increases due to the evanescent contribution such that it exceeds the blackbody limit by several orders of magnitude.

The formalism for thermal emission by a system with nonequilibrium carriers was provided by Greffet *et al.* [37] asserting that the subsystem temperature of a carrier in nonequilibrium should be used along with its contribution to the dielectric function. Thus, the emission of the metallic layer is dominated by the free-electron contribution during nonequilibrium and before electron-phonon thermalization (i.e., at timescales less than ~10 ps after an electronic excitation). At this short timescale, there is an opportunity to sink this heat before the bulk system reaches a high-entropy equilibrium dominated by diffusive processes. The dielectric behavior of free electrons is described by the Drude model as

$$\varepsilon_m(\omega) = 1 - \frac{\omega_p^2}{\omega^2 + i\omega\Gamma_{\mathrm{tot}}}, \tag{1}$$

where ω_p is the plasma frequency and Γ_{tot} is the total electronic scattering term. As the Drude model predicts a broadband dielectric function across the infrared region of the spectrum (where most of the RHT occurs), the spectral energy density due to thermal emission by the metallic

layer also exhibits a broadband behavior, as shown in Fig. 1(b) for gold, as an example.

When considering a nonequilibrium system with elevated electron temperatures, we need to investigate the scope of the Drude oscillator parameters (i.e., ω_p and Γ_{tot}), which vary noticeably with electron temperature. The strength of the Drude oscillator is given by the plasma frequency, defined as

$$\omega_p(T_e) = \sqrt{\frac{n_e(T_e)e^2}{4\pi m^*(T_e)\epsilon_0}}, \tag{2}$$

where e and ϵ_0 are the elementary charge and free-space permittivity, respectively. The parameters which depend on the electron temperature, T_e, are the effective mass (m^*) and the number density of electrons (n_e) given by integrating the occupied density of electronic states over all energies. The temperature dependencies of m^* and n_e can be computed from the total electron density of states (eDOS) and the chemical potential, μ, detailed in Supplemental Material [38].

There is also a sizable increase in the total electronic scattering rate, Γ_{tot}, at high temperatures due to the increase in average collisions experienced by electrons at the broadened Fermi surface. The classic Drude model assumes independent electrons, but at the nanoscale, elastic collisions between electrons and boundaries become significant. To account for this effect, we extend the Drude model using Matthiessen's rule [43], providing a more accurate total relaxation time, Γ_{tot}, as

$$\Gamma_{\text{tot}} = \Gamma_{ee} + \Gamma_{ep} + \Gamma_{eb}, \tag{3}$$

where Γ_{ee}, Γ_{ep}, and Γ_{eb} are the electron-electron, electron-phonon, and electron-boundary scattering rates, respectively. Each of these rates can be calculated from first principles under the theories of Fermi liquid theory [44,45], electronic Cerenkov radiation of sound waves [46], and inelastic electron scattering from a vibrating boundary [47], with the inputs taken from Refs. [31,48] (see Supplemental Material for details [38]). Throughout the simulations performed in this work, we consider a metal film thickness of 10 nm with a "cold" lattice, i.e., $T_p = 300$ K. This assumption represents the initial transient phase of strong electron-phonon nonequilibrium following an intense electronic excitation. During this scenario, T_e can reach thousands of Kelvin while T_p remains nearly constant on the timescale of picoseconds due to the relatively slow electron-phonon energy exchange. This isolates the impact of hot electrons on radiative heat flux in nonequilibrium conditions, such as after ultrafast laser excitation [49] or during high-power electronic device operation [27,50].

The temperature dependence of these scattering rates along with the total scattering rate in three representative

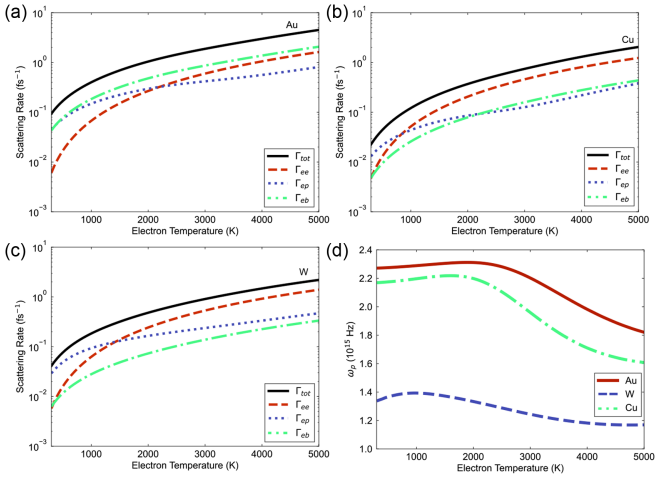

FIG. 2. (a)–(c) Electron-electron, electron-phonon, electron-boundary, and total scattering rates in a film of gold, copper, and tungsten, respectively. The thickness of the film is set to 10 nm. (d) Electron temperature trend of the plasma frequency for each metal film.

metals (i.e., Au, Cu, and W) are shown in Figs. 2(a)–2(c). At the low-temperature limit of $T_e \sim 300$ K, the dominant mechanism is electron-phonon scattering as the system is close to equilibrium and the phonons scatter more readily since they have higher heat capacity than the free electrons. At electron temperatures higher than 2500 K, this trend inverts, and the self-interaction of the electronic sea, i.e., the electron-electron scattering, dominates over the electron-phonon counterpart. While all three metal films show similar electron-electron scattering rates, the gold film exhibits a higher electron-phonon scattering rate than copper and tungsten. Although gold has the lowest electron-phonon coupling among these three metals [31], the electron-phonon scattering rate is the highest since gold has the lowest sound speed (see Supplemental Material [38]). Additionally, the lower sound speed in gold causes electron-boundary scattering to be the dominant contributing mechanism to the total scattering.

Figure 2(d) shows the trends in the plasma frequencies, where Au and Cu exhibit a characteristic downturn, in contrast to the relatively stable trend in tungsten. Gold and copper are both noble metals that conduct via their outer s-band at lower temperatures. The general trend for these noble metals is a trend upward in number density at moderate electron temperatures ($T_e < 2000$ K) due to Fermi smearing into the d-bands, resulting in a increase in ω_p. However, at higher temperatures, the tail of Fermi smearing starts to gain access to the heavy d-bands. Hence, while the number density keeps increasing, the competing effect of the effective mass of the d-band electrons dominates the trend at $T_e > 2000$ K and thus, decreases ω_p. Tungsten, a non-noble transition metal, has a much smoother trend with electron temperature due to the d-bands participating in conduction throughout the temperature ranges simulated.

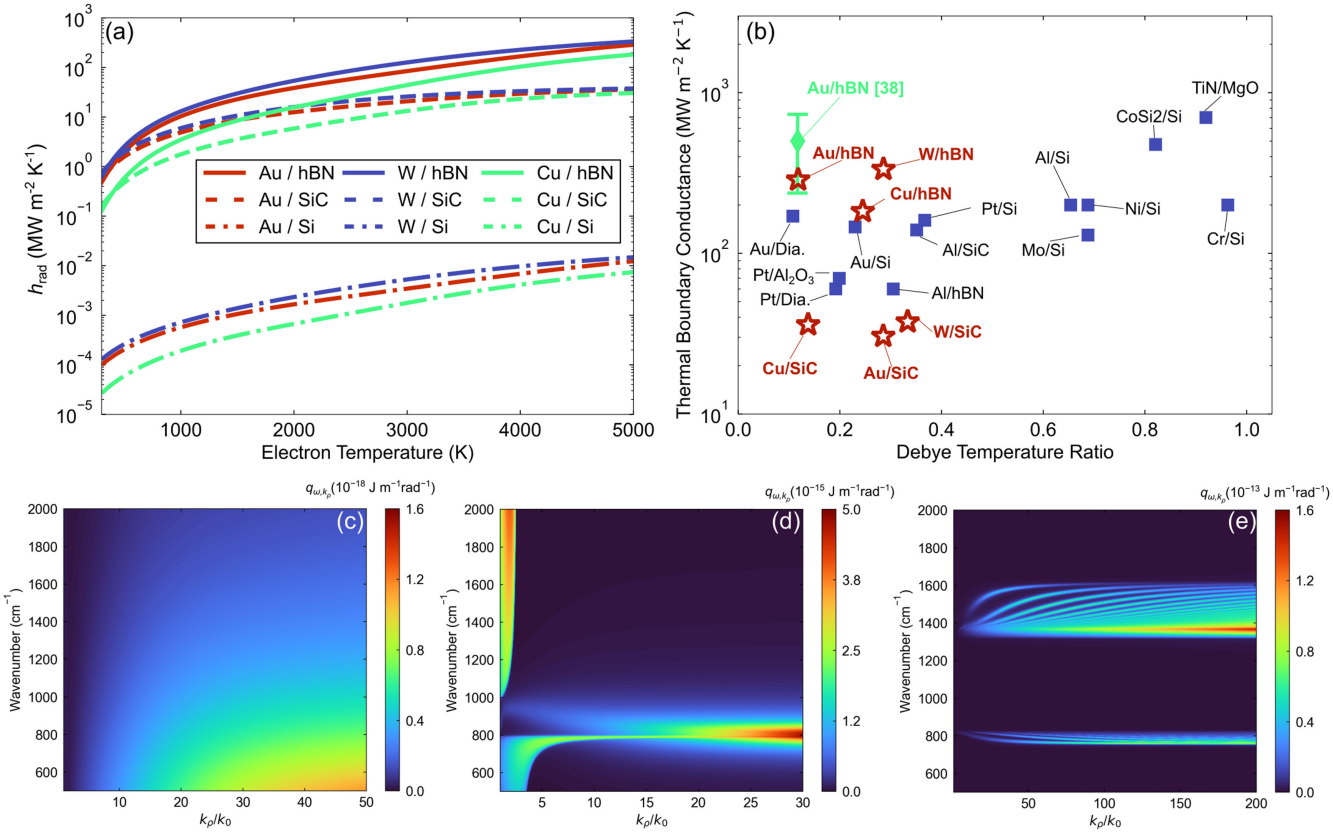

FIG. 3. (a) FED predictions of radiative TBC at varying electron temperatures. The highest h_{rad} can be expected from the absorption into high-wave-vector phonon polaritons in hBN and SiC. The lack of polaritonically active optical modes in the Si results in small values of h_{rad} during nonequilibrium. (b) Comparison of nonequilibrium h_{rad} calculated in this work (red stars) with measured TBC values at nonequilibrium (green diamond [57]) as well as room-temperature phonon-phonon TBCs (black squares [3]). The values of TBC are plotted against the ratio of the film and substrate Debye temperatures, which gives a first approximation to the effective acoustic impedance matching used to estimate the efficiency of interfacial phonon transport. (c)–(e) Representative dispersion of evanescent radiative spectral heat flux per unit wave vector transferred from the metal to the substrate in the cases of 10-nm Au film with $T_e = 5000$ K on Si, 3C-SiC, and hBN, respectively.

With the Drude parameters calculated at high electron temperatures, we can utilize FED to determine the radiative heat flux associated with propagating and evanescent modes across the interface between the metallic thin film and an insulator substrate [51,52], as described in Appendix C. This flux is then used to calculate the thermal boundary conductance with $\Delta T = T_e - T_p$. We considered three semi-infinite substrates (i.e., Si, 3C-SiC, and hBN) with different dielectric behaviors in the infrared region. While Si does not support any optical features that would significantly enhance the radiative heat flux, 3C-SiC and hBN can support evanescent polaritonic modes [53] that cause a resonant increase in the heat flux. 3C-SiC is an isotropic polar wide-bandgap semiconductor with a large transverse optical (TO) absorption peak in the infrared region and supports phonon polaritons [36,54,55]. Also, hBN is an anisotropic uniaxial medium with different in-plane and cross-plane dielectric functions. hBN possesses two hyperbolic spectral regions, in which the in-plane and cross-plane dielectric functions have opposite signs and hyperbolic phonon polaritons may be excited, resulting in a broadband enhancement of radiative heat flux [56]. The dielectric functions of these substrate materials are found using available literature parameters [41,53].

Figure 3(a) shows the calculated results for evanescent radiative conductances, h_{rad}, for all nine interfaces. We observe a two-order-of-magnitude increase in the interfacial radiative conductance at high electron temperatures when compared to near-equilibrium conditions (i.e., low T_e). The magnitude of these radiative conductances, however, is only significant for polar substrates with strong dipole oscillators supporting strong resonant modes at high wave vectors. For polaritonically active substrates, the value of h_{rad} approaches the order of conductive transport (~ 100s MW m^{-2} K^{-1}) [26] at electron temperatures above 3000 K. Figure 3(b) presents a range of literature values for total TBC measured during local thermodynamic equilibrium, i.e., $T_e = T_p = 300$ K. Comparing our calculated values at $T_e = 5000$ K to the literature values, we see that h_{rad} can be the dominant mechanism under nonequilibrium.

Au and W show the highest evanescent transfer to polaritonic substrates, up to 333.7 $\mathrm{MW\,m^{-2}\,K^{-1}}$ at $T_e = 5000$ K. In the case of tungsten, this is due to the dramatically lower ω_p of the metal [see Fig. 2(d)], resulting in a small negative dielectric function allowing more modes through the metal-insulator interface. Gold compensates for a high ω_p with overall higher scattering rates which broaden the envelope of evanescent modes and results in a comparable flux to that of W (see Appendix B of Supplemental Material for sensitivity of heat flux to each Drude term [38]).

We focus on electron temperatures up to 5000 K to model scenarios of strong electron-phonon nonequilibrium, where electrons transiently reach high temperatures before thermalization with the lattice. The only measured value of radiative TBC in such nonequilibrium conditions is for the Au/hBN interface, reported by Hutchins *et al.* [57]. The ultrafast heat transfer measurement described in Ref. [57], involving evanescent coupling between hot electrons in gold and hyperbolic phonon polaritons in hBN, aligns with the theoretical predictions presented here. The reported "polaritonic interface conductance" of 500 $\mathrm{MW\,m^{-2}\,K^{-1}}$ at high electron temperatures agrees within uncertainty with our calculated h_{rad}.

To elucidate the effect of substrate on the radiative flux, we show the spectral heat flux per unit k_ρ emitted by the gold film with $T_e = 5000$ K into the three substrates in Figs. 3(c)–3(e). The absorption from the Drude oscillator in Si results in a weak broadband heat flux. In the case of 3C-SiC [Fig. 3(d)], the radiative heat flux is dominated by the excitation of bulk phonon polaritons at lower wave vectors and the TO absorption at high wave vectors. The latter occurs at a narrow spectral region resulting in a quasi-monochromatic heat flux between the metallic layer and the substrate. The transfer of flux across the interface is dictated by the allowed electromagnetic modes at each side of the interface; thus the strongest optical phonons and/or polaritons result in the most radiative flow. The metal-substrate paring that resulted in the highest h_{rad} was that of W on hBN due to the intense absorption into the high-wave-vector hyperbolic phonon polaritons excited within two hyperbolic regions of hBN, as illustrated in Fig. 3(e). These hyperbolic modes result in a directional volumetric sinking of heat from the emitting metal layer. Such enhancement of radiative interfacial heat transport under strong electron-phonon nonequilibrium has potential applications in hot electron transistors [58,59], thermal switching [60,61], thermophotovoltaics [14,62,63], and nanophotonic devices [15,16,64]. This work provides a foundation for designing advanced materials and devices that leverage these radiative mechanisms for efficient energy transduction. The presented results in Fig. 3 show that, while the photonic energy transfer across solid-state dielectric interfaces is often overlooked when tuning the efficiency of thermal transport, the evanescent flux emitted can become significant in cases of extreme nonequilibrium.

In summary, we investigated evanescent RHT under extreme nonequilibrium in various thin film metals in contact with several dielectric absorbers. Using fluctuational electrodynamics, we predicted interfacial radiative conductance for electron temperatures ranging from 300 to 5000 K. We found that polaritonic substrate supporting surface or hyperbolic phonon polaritons in the infrared region could achieve radiative conductance comparable to its conductive counterpart. The highest conductance was observed for a tungsten film on hBN at high electron temperature due to hyperbolic phonon polaritons, surpassing 300 $\mathrm{MW\,m^{-2}\,K^{-1}}$ and rivaling typical phonon-phonon interfacial conductances. The trends observed in radiative TBC suggest that electrons impinging on an insulating interface can emit energy not only via e-p coupling but via the transduction of thermal energy into polaritonic and photonic modes of the absorber, providing an additional pathway for thermal transport and energy transduction at the nanoscale.

Acknowledgments—This work is supported by the Office of Naval Research under Grant No. N00014-23-1-2630.

[1] E. T. Swartz and R. O. Pohl, Thermal boundary resistance, Rev. Mod. Phys. **61**, 605 (1989).
[2] P. E. Hopkins, Thermal transport across solid interfaces with nanoscale imperfections: Effects of roughness, disorder, dislocations, and bonding on thermal boundary conductance, ISRN Mech. Eng. **2013**, 682586 (2013).
[3] A. Giri, M. V. Tokina, O. V. Prezhdo, and P. E. Hopkins, Electron–phonon coupling and related transport properties of metals and intermetallic alloys from first principles, Mater. Today Phys. **12**, 100175 (2020).
[4] C. Monachon, L. Weber, and C. Dames, Thermal boundary conductance: A materials science perspective, Annu. Rev. Mater. Res. **46**, 433 (2016).
[5] J. Chen, X. Xu, J. Zhou, and B. Li, Interfacial thermal resistance: Past, present, and future, Rev. Mod. Phys. **94**, 025002 (2022).
[6] A. Giri, S. G. Walton, J. Tomko, N. Bhatt, M. J. Johnson, D. R. Boris, G. Lu, J. D. Caldwell, O. V. Prezhdo, and P. E. Hopkins, Ultrafast and nanoscale energy transduction mechanisms and coupled thermal transport across interfaces, ACS Nano **17**, 14253 (2023).
[7] S.-A. Biehs, M. Tschikin, and P. Ben-Abdallah, Hyperbolic metamaterials as an analog of a blackbody in the near field, Phys. Rev. Lett. **109**, 104301 (2012).
[8] Y. Guo and Z. Jacob, Fluctuational electrodynamics of hyperbolic metamaterials, J. Appl. Phys. **115**, 234306 (2014).
[9] A. Principi, M. B. Lundeberg, N. C. Hesp, K. J. Tielrooij, F. H. Koppens, and M. Polini, Super-Planckian electron cooling in a van der Waals stack, Phys. Rev. Lett. **118**, 126804 (2017).
[10] E. G. Cravalho, C. L. Tien, and R. P. Caren, Effect of small spacings on radiative transfer between two dielectrics, J. Heat Transfer **89**, 351 (1967).

[11] V. Chiloyan, J. Garg, K. Esfarjani, and G. Chen, Transition from near-field thermal radiation to phonon heat conduction at sub-nanometre gaps, Nat. Commun. **6**, 6755 (2015).
[12] J. Zhang, K. Shi, L. Lu, D. Feng, H. Liu, and X. Wu, Experiments on near-field radiative heat transfer: A review, Clean Energy Sci. Technol. **1**, 45 (2023).
[13] M. Ghashami, A. Jarzembski, M. Lim, B. J. Lee, and K. Park, Experimental exploration of near-field radiative heat transfer, Annu. Rev. Heat Transf. **23**, 13 (2020).
[14] A. Lenert, D. M. Bierman, Y. Nam, W. R. Chan, I. Celanović, M. Soljačić, and E. N. Wang, A nanophotonic solar thermophotovoltaic device, Nat. Nanotechnol. **9**, 126 (2014).
[15] W. A. Challener, C. Peng, A. V. Itagi, D. Karns, W. Peng, Y. Peng, X. Yang, X. Zhu, N. J. Gokemeijer, Y.-T. Hsia, G. Ju, R. E. Rottmayer, M. A. Seigler, and E. C. Gage, Heat-assisted magnetic recording by a near-field transducer with efficient optical energy transfer, Nat. Photonics **3**, 220 (2009).
[16] B. C. Stipe, T. C. Strand, C. C. Poon, H. Balamane, T. D. Boone, J. A. Katine, J.-L. Li, V. Rawat, H. Nemoto, A. Hirotsune, O. Hellwig, R. Ruiz, E. Dobisz, D. S. Kercher, N. Robertson, T. R. Albrecht, and B. D. Terris, Magnetic recording at 1.5 Pb m-2 using an integrated plasmonic antenna, Nat. Photonics **4**, 484 (2010).
[17] Y. De Wilde, F. Formanek, R. Carminati, B. Gralak, P.-A. Lemoine, K. Joulain, J.-P. Mulet, Y. Chen, and J.-J. Greffet, Thermal radiation scanning tunnelling microscopy, Nature (London) **444**, 740 (2006).
[18] A. Kittel, U. F. Wischnath, J. Welker, O. Huth, F. Rüting, and S.-A. Biehs, Near-field thermal imaging of nanostructured surfaces, Appl. Phys. Lett. **93**, 193109 (2008).
[19] J.-J. Greffet, R. Carminati, K. Joulain, J.-P. Mulet, S. Mainguy, and Y. Chen, Coherent emission of light by thermal sources, Nature (London) **416**, 61 (2002).
[20] A. C. Jones, B. T. O'Callahan, H. U. Yang, and M. B. Raschke, The thermal near-field: Coherence, spectroscopy, heat-transfer, and optical forces, Prog. Surf. Sci. **88**, 349 (2013).
[21] R. Carminati and J.-J. Greffet, Near-field effects in spatial coherence of thermal sources, Phys. Rev. Lett. **82**, 1660 (1999).
[22] J.-P. Mulet, K. Joulain, R. Carminati, and J.-J. Greffet, Enhanced radiative heat transfer at nanometric distances, Microscale Thermophys. Eng. **6**, 209 (2002).
[23] H. Iizuka and S. Fan, Analytical treatment of near-field electromagnetic heat transfer at the nanoscale, Phys. Rev. B **92**, 144307 (2015).
[24] M. Francoeur, M. P. Mengüç, and R. Vaillon, Spectral tuning of near-field radiative heat flux between two thin silicon carbide films, J. Phys. D **43**, 075501 (2010).
[25] S. M. Rytov, i. A. Kravtsov, and V. I. Tatarskii, *Principles of Statistical Radiophysics* (Springer-Verlag, Berlin, 1987).
[26] A. Giri and P. E. Hopkins, A review of experimental and computational advances in thermal boundary conductance and nanoscale thermal transport across solid interfaces, Adv. Funct. Mater. **30**, 1903857 (2020).
[27] E. Minamitani, *Ab initio* analysis for the initial process of Joule heating in semiconductors, Phys. Rev. B **104**, 085202 (2021).
[28] N. W. Ashcroft and N. D. Mermin, *Solid State Physics* (Rinehart and Winston, Holt, 1976).
[29] W. Cai, M. C. Marchetti, and M. Lax, Nonequilibrium electron-phonon scattering in semiconductor heterojunctions, Phys. Rev. B **34**, 8573 (1986).
[30] K. Král, Electrophonon resonance in Al x Ga 1—x As-GaAs quasi-two-dimensional quantum wells, Phys. Rev. B **50**, 7640 (1994).
[31] Z. Lin, L. V. Zhigilei, and V. Celli, Electron-phonon coupling and electron heat capacity of metals under conditions of strong electron-phonon nonequilibrium, Phys. Rev. B **77**, 075133 (2008).
[32] A. Giri, J. T. Gaskins, B. M. Foley, R. Cheaito, and P. E. Hopkins, Experimental evidence of excited electron number density and temperature effects on electron-phonon coupling in gold films, J. Appl. Phys. **117**, 044305 (2015).
[33] P. E. Hopkins and D. A. Stewart, Contribution of d-band electrons to ballistic transport and scattering during electron-phonon nonequilibrium in nanoscale Au films using an *ab initio* density of states, J. Appl. Phys. **106**, 053512 (2009).
[34] S. I. Anisimov, B. L. Kapeliovich, and T. L. Perel'man, Electron emission from the metal surfaces induced by ultrashort lasers pulses, Zh. Ehksp. Teor. Fiz. **66**, 776 (1974).
[35] A. Giri, B. M. Foley, and P. E. Hopkins, Influence of hot electron scattering and electron–phonon interactions on thermal boundary conductance at metal/nonmetal interfaces, J. Heat Transfer **136**, 092401 (2014).
[36] K. Joulain, J.-P. Mulet, F. Marquier, R. Carminati, and J.-J. Greffet, Surface electromagnetic waves thermally excited: Radiative heat transfer, coherence properties and Casimir forces revisited in the near field, Surf. Sci. Rep. **57**, 59 (2005).
[37] J.-J. Greffet, P. Bouchon, G. Brucoli, and F. Marquier, Light emission by nonequilibrium bodies: Local Kirchhoff law, Phys. Rev. X **8**, 021008 (2018).
[38] See Supplemental Material at http://link.aps.org/supplemental/10.1103/PhysRevLett.134.186302 for the temperature dependency of electronic properties, temperature-dependent electron-phonon coupling, substrate optical constants, and sensitivity of radiative conductance to the electronic properties, which also includes Refs. [39–42].
[39] G. Kresse, J. Furthmüller, and J. Hafner, Theory of the crystal structures of selenium and tellurium: The effect of generalized-gradient corrections to the local-density approximation, Phys. Rev. B **50**, 13181 (1994).
[40] W. M. Haynes, *CRC Handbook of Chemistry and Physics*, 65th ed. (CRC Press, Boca Raton, FL, 2016).
[41] E. D. Palik, *Handbook of Optical Constants of Solids* (Academic Press, New York, 1998).
[42] J. D. Caldwell, A. V. Kretinin, Y. Chen, V. Giannini, M. M. Fogler, Y. Francescato, C. T. Ellis, J. G. Tischler, C. R. Woods, A. J. Giles, M. Hong, K. Watanabe, T. Taniguchi, S. A. Maier, and K. S. Novoselov, Sub-diffractional volume-confined polaritons in the natural hyperbolic material hexagonal boron nitride, Nat. Commun. **5**, 5221 (2014).
[43] M. R. Islam *et al.*, Evaluating size effects on the thermal conductivity and electron-phonon scattering rates of copper

thin films for experimental validation of Matthiessen's rule, Nat. Commun. **15**, 9167 (2024).
[44] V. Gasparov and R. Huguenin, Electron-phonon, electron-electron and electron-surface scattering in metals from ballistic effects, Adv. Phys. **42**, 393 (1993).
[45] D. Pines and D. Bohm, A collective description of electron interactions: II. Collective vs individual particle aspects of the interactions, Phys. Rev. **85**, 338 (1952).
[46] M. I. Kaganov, E. M. Lifshitz, and L. V. Tanatarov, Relaxation between electrons and the crystalline lattice, Sov. Phys.-JETP **4**, 173 (1957).
[47] A. V. Sergeev, Electronic Kapitza conductance due to inelastic electron-boundary scattering, Phys. Rev. B **58**, R10199 (1998).
[48] P. Giannozzi *et al.*, QUANTUM ESPRESSO: A modular and open-source software project for quantum simulations of materials, J. Phys. Condens. Matter **21**, 395502 (2009).
[49] J. Hohlfeld, S.-S. Wellershoff, J. Güdde, U. Conrad, V. Jähnke, and E. Matthias, Electron and lattice dynamics following optical excitation of metals, Chem. Phys. **251**, 237 (2000).
[50] S. Yngvesson, *Microwave Semiconductor Devices* (Springer US, Boston, MA, 1991).
[51] M. Francoeur, M. Pinar Mengüç, and R. Vaillon, Solution of near-field thermal radiation in one-dimensional layered media using dyadic Green's functions and the scattering matrix method, J. Quant. Spectrosc. Radiat. Transfer **110**, 2002 (2009).
[52] H. Salihoglu, V. Iyer, T. Taniguchi, K. Watanabe, P. D. Ye, and X. Xu, Energy transport by radiation in hyperbolic material comparable to conduction, Adv. Funct. Mater. **30**, 1905830. (2020).
[53] A. J. Giles, S. Dai, I. Vurgaftman, T. Hoffman, S. Liu, L. Lindsay, C. T. Ellis, N. Assefa, I. Chatzakis, T. L. Reinecke, J. G. Tischler, M. M. Fogler, J. H. Edgar, D. N. Basov, and J. D. Caldwell, Ultralow-loss polaritons in isotopically pure boron nitride, Nat. Mater. **17**, 134 (2018).
[54] R. Pouria, P. K. Chow, T. Tiwald, S. Zare, and S. Edalatpour, Far-field thermal radiation from short-pitch silicon-carbide nanopillar arrays, Appl. Phys. Lett. **121**, 131702 (2022).
[55] S. Zare, R. Pouria, P. K. Chow, T. Tiwald, C. P. Tripp, and S. Edalatpour, Probing near-field thermal emission of localized surface phonons from silicon carbide nanopillars, ACS Photonics **10**, 401 (2023).
[56] S. Zare, C. P. Tripp, and S. Edalatpour, Measurement of near-field thermal emission spectra using an internal reflection element, Phys. Rev. B **100**, 235450 (2019).
[57] W. Hutchins, S. Zare, D. M. Hirt, J. A. Tomko, J. R. Matson, K. Diaz-Granados, M. Long, M. He, T. Pfeifer, J. Li, J. H. Edgar, J.-P. Maria, J. D. Caldwell, and P. E. Hopkins, Ultrafast evanescent heat transfer across solid interfaces via hyperbolic phonon–polariton modes in hexagonal boron nitride, Nat. Mater. (2025), 10.1038/s41563-025-02154-5.
[58] M. Heiblum and M. V. Fischetti, Ballistic hot-electron transistors, IBM J. Res. Dev. **34**, 530 (1990).
[59] S. Vaziri, A. D. Smith, M. Östling, G. Lupina, J. Dabrowski, G. Lippert, W. Mehr, F. Driussi, S. Venica, V. Di Lecce, A. Gnudi, M. König, G. Ruhl, M. Belete, and M. C. Lemme, Going ballistic: Graphene hot electron transistors, Solid State Commun. **224**, 64 (2015).
[60] B. Yang, B. Song, F. J. G. de Abajo, and Q. Dai, Ultrafast thermal switching enabled by transient polaritons, ACS Nano **19**, 1490 (2025).
[61] N. H. Thomas, M. C. Sherrott, J. Broulliet, H. A. Atwater, and A. J. Minnich, Electronic modulation of near-field radiative transfer in graphene field effect heterostructures, Nano Lett. **19**, 3898 (2019).
[62] R. Mittapally, B. Lee, L. Zhu, A. Reihani, J. W. Lim, D. Fan, S. R. Forrest, P. Reddy, and E. Meyhofer, Near-field thermophotovoltaics for efficient heat to electricity conversion at high power density, Nat. Commun. **12**, 4364 (2021).
[63] R. Mittapally, A. Majumder, P. Reddy, and E. Meyhofer, Near-field thermophotovoltaic energy conversion: Progress and opportunities, Phys. Rev. Appl. **19**, 037002 (2023).
[64] S. Kim, B. Zhang, Z. Wang, J. Fischer, S. Brodbeck, M. Kamp, C. Schneider, S. Höfling, and H. Deng, Coherent polariton laser, Phys. Rev. X **6**, 011026 (2016).

End Matter

Appendix A: Plasma frequency calculation—The plasma frequency of the metallic thin film was found as described in Eq. (2) of the Letter and is given by

$$\omega_p(T_e) = \sqrt{\frac{n_e(T_e)e^2}{4\pi m^*(T_e)\epsilon_0}}, \tag{A1}$$

where ε_0 and e are the vacuum permittivity and electron charge, respectively. The temperature-dependent parameters in this equation are n_e and m^*, which represent the number density and effective mass of electrons, respectively. The number density of electrons, n_e, was calculated from the integration of the occupied density of states (ODOS), $g(\epsilon, T_e)$, across all energies, ϵ. The ODOS was obtained by multiplying the ground state density of states (DOS), $D(\epsilon)$, by the Fermi Dirac distribution, $f_{\mathrm{FD}}(\epsilon, T_e)$, as

$$g(\epsilon, T_e) = D(\epsilon).f_{\mathrm{FD}}(\epsilon, T_e). \tag{A2}$$

To find DOS for each metal film, we conducted self-consistent field calculations in the Quantum ESPRESSO package [48] using a $8 \times 8 \times 8$ grid of k-points. The number density of states was then calculated as

$$n_e(T_e) = \int_0^\infty g(\epsilon, T_e)d\epsilon = \int_0^\infty D(\epsilon)f(\epsilon, T_e)d\epsilon. \tag{A3}$$

The thermal effective mass for each metal film was retrieved by the Ashcroft and Mermin formulation [43] as

$$m^*(T_e) = \frac{\gamma(T_e)}{\gamma_{\text{free}}(T_e)}, \tag{A4}$$

where γ and γ_{free} are the actual and free-electron Sommerfeld coefficients, respectively. The values of γ and γ_{free} for each metal film at given T_e are found as

$$\gamma(T_e) = \frac{C_e(T_e)}{T_e} \tag{A5}$$

$$\gamma_{\text{free}}(T_e) = \frac{\pi^2 n_e(T_e) k_b^2}{2\mu(T_e)}, \tag{A6}$$

where C_e is the heat capacity of electrons, μ is the chemical potential, and k_b is the Boltzmann constant. Finally, with electron effective mass and number density calculated, the plasma frequency of each metal film was found.

Appendix B: Electron scattering rate calculation—The electron-electron scattering rate was obtained using the Fermi liquid theory formulation, described in Ref. [44], as

$$\Gamma_{ee}(T_e) = \frac{e^4 k_F^2}{16\pi^3 \hbar^4 \varepsilon_0^2 v_F^3 q_s^2}\left[\frac{2k_F}{4k_F + q_s^2} + \frac{1}{q_s}\arctan\left(\frac{2k_F}{q_s}\right)\right] \times \left[\pi^2 + \left(\frac{\epsilon - \epsilon_F - \mu}{k_B T_e}\right)^2\right](k_B T_e)^2, \tag{B1}$$

where k_F and v_F are the Fermi momentum and velocity, respectively, and are related to the Fermi energy, ϵ_F, and the rest mass of the electron, m_e, as

$$k_F = \sqrt{2m_e\epsilon_F}/\hbar \tag{B2}$$

$$v_F = k_F\hbar/m_e, \tag{B3}$$

where $\hbar$ and m_e are the reduced Planck constant and the rest mass of an electron, respectively. Also, q_s represents the screening length of the electron, that is, the distance at which the electrostatic force of the electron is attenuated. The screening length in the above formulation is given by Bohm and Pines [45] as

$$q_{\text{BP}}^{-1} = \frac{4\pi\varepsilon_0\hbar^2 1.47 r_s^{1/2}}{e^2 m_e}, \tag{B4}$$

where r_s is the inter-electron distance of the simulated metal given by

$$r_s = \frac{4\pi\varepsilon_0\hbar^2(3/4\pi n_e)^{1/3}}{e^2 m_e}. \tag{B5}$$

The electron-phonon scattering rate for each metal film was found by following the formula reported in Ref. [46]:

$$\Gamma_{ep}^{-1}(T_e) = \frac{\pi^2}{6}\frac{m^*(T_e)C_s^2 n_e(T_e)}{G_{ep}(T_e)T_e}, \tag{B6}$$

where C_s is the Debye sound speed of the metal given by

$$\frac{3}{C_s^3} = \frac{1}{u_L^3} + \frac{2}{u_T^3}. \tag{B7}$$

In Eq. (S13), u_L and u_T are the longitudinal and transverse sound speeds, respectively. The values of the longitudinal and transverse sound speeds for each simulated metal can be found in Table S1.

To find the electron-boundary scattering rate, we followed the formula reported in Ref. [47] as

$$\Gamma_{eb}(T_e) = \frac{3\pi}{35\zeta(3)\Gamma_{ep}^{-1}(T_e)q_T t}\left[1 + 2\left(\frac{u_L}{u_T}\right)^3\right], \tag{B8}$$

where ζ is the Riemann-Zeta function, q_T is the wave vector of a thermal longitudinal phonon ($q_T = T_p/u_L$), and t is the thickness of the metal film.

Appendix C: Radiative heat flux calculation—Figure 4 represents a schematic of the radiative heat transfer problem under consideration as a one-dimensional layered configuration with two solid-state layers. In this configuration, layer 1 is a thin metallic film emitter (with a thickness of t) with a bulk vacuum layer on top, and layer 2 is a receiving dielectric half-space. The dielectric response of each layer is described using a frequency-dependent dielectric function, $\varepsilon(\omega) = \varepsilon'(\omega) + i\varepsilon''(\omega)$. As layers are infinitely long in the x and y directions, we only consider heat flux along the z axis. Utilizing the framework of fluctuational electrodynamics [51] in Cartesian coordinates, the spectral radiative heat transfer (q_ω) from the thin film to the substrate is given by the time-averaged z-component of the Poynting vector as

$$q_\omega = 2\mathbf{Re}[\langle E_x H_y^* - E_y H_x^*\rangle], \tag{C1}$$

where $*$ denotes the complex conjugate. Here, E_x and E_y (H_x and H_y) are the x- and y-components of the electric (magnetic) field $\mathbf{E}$ ($\mathbf{H}$), respectively, thermally

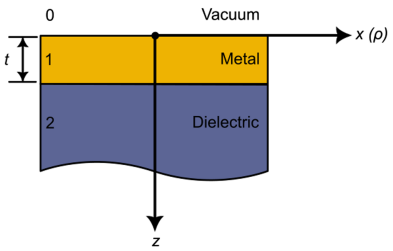

FIG. 4. Schematic diagram of the configuration considered for radiative heat flux calculations.

emitted by the thin film. These thermally emitted fields can be found using the fluctuation-dissipation theorem and the formalism of dyadic Green's function (DFG) [51]. By adopting a polar coordinate system and considering the azimuthal symmetry of the configuration, the radiative heat flux is then found as

$$q_\omega = \int_0^{k_{\max}} \frac{k_0^2 \Theta(\omega, T)}{\pi^2} \times \mathbf{Re}\left[i \int_0^t \sum_{\alpha=\rho,\theta,z} \varepsilon''(\omega) \left(\mathbf{g}^E_{\rho\alpha} \mathbf{g}^{H^*}_{\theta\alpha} - \mathbf{g}^E_{\theta\alpha} \mathbf{g}^{H^*}_{\rho\alpha} \right) dz \right] k_\rho \mathrm{d}k_\rho, \tag{C2}$$

where Θ is the mean energy of electromagnetic states, k_0 is the vacuum wave vector, and k_ρ is the parallel (relative to the surface) component of the wave vector. In this study, we set the upper wave vector limit $k_{\max} = \pi/a$, where a is the lattice constant of the material. This choice reflects the physical limit imposed by the material's atomic structure and photonic response [52]. Also, $\mathbf{g}$ is the Weyl component of DGFs, given by

$$\mathbf{g}^E(\omega, k_\rho) = \frac{i}{2k_{z1}} \begin{bmatrix} \left(A_2^{TE} \hat{\mathbf{s}}\,\hat{\mathbf{s}} + A_2^{TM} \hat{\mathbf{p}}_2^+ \hat{\mathbf{p}}_1^+ \right) e^{-ik_{z1}z} \\ + \left(B_2^{TE} \hat{\mathbf{s}}\,\hat{\mathbf{s}} + B_2^{TM} \hat{\mathbf{p}}_2^- \hat{\mathbf{p}}_1^+ \right) e^{-ik_{z1}z} \\ + \left(C_2^{TE} \hat{\mathbf{s}}\,\hat{\mathbf{s}} + C_2^{TM} \hat{\mathbf{p}}_2^+ \hat{\mathbf{p}}_1^- \right) e^{ik_{z1}z} \\ + \left(D_2^{TE} \hat{\mathbf{s}}\,\hat{\mathbf{s}} + D_2^{TM} \hat{\mathbf{p}}_2^- \hat{\mathbf{p}}_1^- \right) e^{ik_{z1}z} \end{bmatrix} \tag{C3}$$

$$\mathbf{g}^H(\omega, k_\rho) = \frac{k_2}{2k_{z1}} \begin{bmatrix} \left(A_2^{TE} \hat{\mathbf{p}}_2^+ \hat{\mathbf{s}} - A_2^{TM} \hat{\mathbf{s}} \hat{\mathbf{p}}_1^+ \right) e^{-ik_{z1}z} \\ + \left(B_2^{TE} \hat{\mathbf{p}}_2^- \hat{\mathbf{s}} - B_2^{TM} \hat{\mathbf{s}} \hat{\mathbf{p}}_1^+ \right) e^{-ik_{z1}z} \\ + \left(C_2^{TE} \hat{\mathbf{p}}_2^+ \hat{\mathbf{s}} - C_2^{TM} \hat{\mathbf{s}} \hat{\mathbf{p}}_1^- \right) e^{ik_{z1}z} \\ + \left(D_2^{TE} \hat{\mathbf{p}}_2^- \hat{\mathbf{s}} - D_2^{TM} \hat{\mathbf{s}} \hat{\mathbf{p}}_1^- \right) e^{ik_{z1}z} \end{bmatrix}. \tag{C4}$$

Here, superscript TE and TM refer to the transverse electric and transverse magnetic polarizations, respectively. Also, $\hat{\mathbf{s}}$ and $\hat{\mathbf{p}}_i^\pm$ are respectively the Sipe unit vectors inside the ith layer for TE- and TM-polarizations, given by

$$\hat{\mathbf{s}} = -\hat{\theta} \tag{C5}$$

$$\hat{\mathbf{p}}_i^\pm = \frac{1}{k_i} (\mp k_{z1} \hat{\rho} + k_\rho \hat{z}), \tag{C6}$$

where $k_i = \sqrt{\varepsilon_i} k_0$ and $k_{zi} = \sqrt{k_i^2 - k_\rho^2}$. Finally, the coefficients A_2^γ (B_2^γ) and C_2^γ (D_2^γ) represent the amplitude of waves traveling toward the positive (negative) direction of the z axis in γ-polarization (where $\gamma = TE$ or TM) due to thermal sources emitting in the positive and negative directions of the z axis, respectively. These coefficients can be found using the scattering matrix method described in Ref. [51].